

Spectral Observations at the CILBO Observatory: Calibration and Data Sets

Joe Zender¹, Detlef Koschny^{1,6}, Regina Rudawska², Salvatore Vicinanza³, Stefan Loehle⁴,
Martin Eberhart⁴, Arne Meindl⁷, Hans Smit¹, Lionel Marraffa¹, Rico Landman⁵, and Daphne Stam³

¹European Space Research and Technology Centre (ESA ESTEC), 2200 AG Noordwijk, The Netherlands

²RHEA group/ESA ESTEC, 2200 AG Noordwijk, The Netherlands

³Faculty of Aerospace Engineering, Delft University of Technology, Delft, The Netherlands

⁴IRS, University of Stuttgart, Germany

⁵Leiden Observatory, Leiden University, Postbus 9513, 2300 RA, Leiden, The Netherlands

⁶Chair of Astronautics, TU Munich, 85748 Garching, Germany

⁷MPI for Plasma Physics, 85748 Garching, Germany

Correspondence: Joe Zender (Joe.Zender@esa.int)

Abstract. The Canary Island Long-Baseline Observatory (CILBO) is a double station meteor camera setup located on the Canary Islands and operated by ESA's Meteor Research Group since 2010. Observations of meteors are obtained in the visual wavelength band by intensified video cameras from both stations, supplemented by an intensified video camera mounted with a spectral grating at one of the locations. The cameras observe during cloudless and precipitation-free nights and data are transferred to a main computer located at ESA/ESTEC once a day. The image frames that contain spectral information are calibrated, corrected, and finally processed into line intensity profiles. An ablation simulation, based on Bayesian statistics using a Markov-Chain Monte-Carlo method, allows to determine a parameter space, including the ablation temperatures, chemical elements and their corresponding line intensities, to fit against the line intensity profiles of the observed meteor spectra. The algorithm is presented in this paper and one example is discussed. Several hundred spectra have been processed and made available through the Guest Archive Facility of the Planetary Science Archive of ESA. The data format and meta-data are explained.

1 Introduction

Main insights in the dust composition of our solar system have been obtained during the past decade. Ground-based observations from ultraviolet to radio wavelengths (Snodgrass et al., 2017), space-based telescopes, such as HST (Hadamcik et al., 2016), direct space-based remote-sensing and in-situ observations as obtained by the Rosetta spacecraft during its two year nominal mission lifetime (Rubin et al., 2020; Rivilla et al., 2020; Altwegg et al., 2020), and laboratory analysis of samples returned back to Earth, e.g. by the STARDUST mission (Brownlee, 2014), have provided valuable datasets. A summary of our current knowledge of cometary dust is given in Levasseur-Regourd et al. (2018). For interplanetary dust in general, see Koschny et al. (2019) and references therein. The knowledge of dust allows us to derive further information on e.g. the origin and further evolution of comets (Rubin et al., 2020). Another, indirect way to observe dust is the observation of meteors, thus

the observation of the ablation process of meteoroids through Earth's atmosphere. To allow the chemical analysis of the ablation process, spectral observations are needed and have been successfully demonstrated by several teams in the past decades (Vojáček et al., 2019; Borovička et al., 2005; Abe et al., 2020; Ward, 2017; Madiedo, 2015; Jenniskens et al., 2014; Rudawska et al., 2014; Zender et al., 2002; Matlovič et al., 2019; Vojáček et al., 2019; Zender, 1994).

25 ESA's Meteor Research Group (MRG) maintains a number of cameras acquiring the meteor ablation phenomena in Earth's atmosphere, also known as shooting stars or fireballs for brighter events. A general overview of our activities is given in Koschny et al. (2015a).

Besides supporting campaign-based observations (Koschny et al., 2012; Vaubaillon et al., 2015), the MRG maintains a permanent, double station on the Canary Islands acquiring videos from two distinct locations. The parallel acquisition of meteors
30 allows to derive geometric information through trigonometric algorithms (Koschny et al., 2013a). In one of the CILBO stations, a dedicated camera is equipped with a spectral grating to acquire spectral information of the brightest meteors throughout the ablation process in the Earth atmosphere (Zender et al., 2014).

In this paper, we describe the data reduction process from the acquired images to the final spectra.

A full algorithm to derive meteor spectra was discussed in the middle of the twentieth century by Ceplecha (1971). His
35 observations were executed at the Ondřejov Observatory and based on the usage of photographic cameras acquiring a long-exposure in the visual wavelength regime. Spectral plates or spectral prisms diffracted the lights source, e.g. light from a star or from a meteor, into its spectral components. Once the photographic plate was developed, the light curve was measured using a device named micro-densitometer, e.g. the Mann 1140 or the Lirepho2 micro-densitometer (Lirepho is an acronym for "lichtelektrisches Registrierphotometer" produced by Zeiss). The wavelength identification along the obtained light curve
40 was directly computed due to the availability of the zero-order of the meteor using an earlier algorithm of Ceplecha (1961). Given an in-falling vector (the zero-order of the meteor) on the grating plate, the algorithm computes the (x,y)-position for each wavelength on the focal plane, taking into account rotations between the grating plate reference frame and the optical axes.

Quantitative analysis of meteor spectra was introduced by several observers (Borovicka, 1994a, b; Jenniskens, 2007). The observations and analysis of Borovicka (1994a) identified two main thermal components during the ablation process, a low-
45 temperature component of about 4000 K and a hot-component of 10000 K. Jenniskens (2007) provides a summary of all identified elements and confirms the two thermal components, complemented by the formalism to derive the number densities for chemical elements. The calibration of the wavelength scale is achieved by laboratory measurements using a Mercury-Argon calibration source applied over different source incidence angles. These allow at a later step in the algorithm to confirm the correct distances between potential line intensities of different elements. The wavelength scale is described as nearly
50 linear, which overcomes the problem of the diffraction hyperbola that is the effect of a curved spectrum due to the usage of a non-gnomonic lens. The projection of a meteor spectrum onto an image is only linear under the assumption of an optimal lens (Ceplecha, 1961). The projection of an optimal lens onto an imaging plane, i.e. CCD detector, is gnomonic. In video systems used in the last three decades this is however not given and Dubs and Schlatter (2015) proposes an additional image transformation to transform an acquired image into an gnomonic projection.

55 This paper presents the CILBO observation locations and hardware (Chapter 2) and the data processing steps applied to
the meteor spectra: the individual video frames are radiometrically processed (Chapter 3) and converted into the FITS format.
In case the visual camera has observed the zero-order and the grating camera has observed the first-order spectrum of the
meteor, the wavelengths are computed for each individual frame (Chapter 4) and we obtain a spectral profile. In the following,
an intensity correction is applied to the spectral profile (Chapter 6). To determine the temperature regime and the chemical
60 elements that optimally match the obtained spectral profile, we simulate the spectral response of several elements at different
temperatures and use these simulated values applying the Bayesian methodology (Chapter 7) combined with a Markov-Chain
Monte Carlo (MCMC) sampling. As a result we obtain the line intensities which are then further corrected to the corresponding
number densities of the elements by integrating the column density over the line of sight (Chapter 6).

The data pipeline is then briefly discussed (Chapter 8) using one meteor spectrum. In Chapter 9 we describe the datasets that
65 we make available as supplement to this paper.

2 The Canary Island Long-baseline Observatory: CILBO

2.1 Equipment

The Meteor Research Group (MRG) of the European Space Agency operates the double-station meteor camera system CILBO
(Canary Island Long-Baseline Observatory)(Koschny et al., 2014). Several image-intensified video cameras are operated on
70 Tenerife at the Izaña Observatory, and on La Palma at the Observatorio del Roque de los Muchachos. A photograph of one of
the cameras is shown in Figure 1. Table 1 provides details on the individual cameras and locations.

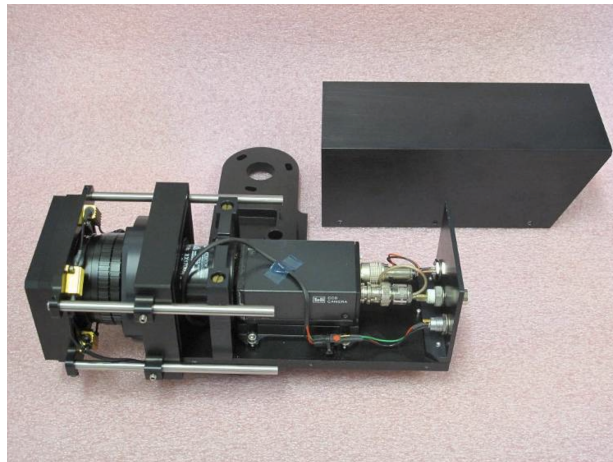


Figure 1. Photograph of one of the intensified video cameras equipped with a grating. The protective cover is removed and visible in the back. Power resistors to heat the grating can be seen on the left.

Table 1. Detailed Information about CILBO stations and its camera setup.

| Tenerife (28.3011°N, -16.5119°W, 2395m) | | | |
|---|----------------|---------------|-----------------------|
| Camera Name | Detector | Optics | Spectral Grating |
| ICC7 | Fujinon CF-25L | 25 mm, f/0.85 | |
| ICC8 | Fujinon CF-25L | 25 mm, f/0.85 | Zeiss, 611 grooves/mm |
| La Palma (28.7600°N, -17.8824°W, 2327m) | | | |
| Camera Name | Detector | Optics | Spectral Grating |
| ICC9 | Fujinon CF-25L | 25 mm, f/0.85 | |

The cameras ICC7 and ICC9 acquire videos with their line-of-sights pointing to a point 100 km above the Earth's surface, at a location between the two islands, at 28.5533°N and -17.1667°W. The so-called spectral camera ICC8 is offset to ICC7 by 23.0° to capture the first order spectrum of meteors passing through the field of view of camera ICC7. A technical overview drawing is shown in Figure 2.

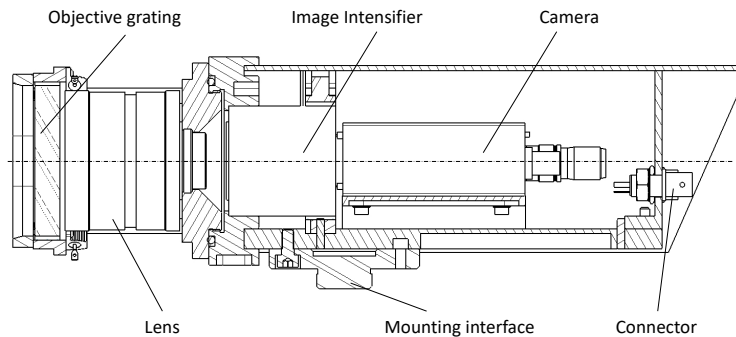


Figure 2. Technical drawing of one of the intensified video cameras.

The camera systems use a low-distortion machine-vision lens from Fujinon, imaging the sky onto the entrance aperture of a second-generation image intensifier (DEP XX-1700). The intensifier has a spectral sensitivity from about 350 to 850 nm. It is fibre-coupled to a charge-coupled device (CCD), which is read out via a Toshiba Teli CS8310Bi PAL video camera. The PAL format has 576×768 pixel². Full frames are read out at a rate of 25 frames per second with 8 bit dynamical accuracy. With the given field of view the pixel scale is 2.3'. A dew remover (type Kendrick) is wrapped around the objective lens to avoid dewing.

Table 2. Meteor events acquired from ICC7 and ICC8 systems since year 2012. Columns *ICC7 Events* and *ICC9 Events* give the number of events recorded by ICC7 and ICC9, respectively. Column *Simultaneous Events* gives the number of events recorded simultaneously by both ICC7 and ICC9. The last row gives the total number of events recorded since 2012.

| <i>Year</i> | <i>ICC7 Events</i> | <i>ICC9 Events</i> | <i>Simultaneous Events</i> | <i>ICC8 Spectral Events</i> |
|--------------|--------------------|--------------------|----------------------------|-----------------------------|
| 2012 | 11312 | 19492 | 4127 | 91 |
| 2013 | 19435 | 10385 | 667 | 110 |
| 2014 | 12647 | 4884 | 195 | 39 |
| 2015 | 18377 | 25423 | 5286 | 54 |
| 2016 | 27481 | 24135 | 2734 | 48 |
| 2017 | 10388 | 9050 | 684 | 12 |
| 2018 | 1150 | 484 | 147 | 1 |
| 2019 | 3088 | 1262 | 335 | 0 |
| 2020 | 0 | 1077 | 0 | 0 |
| <i>Total</i> | 103622 | 96231 | 14174 | 355 |

2.2 Control Software

The core of the software is the detection software MetRec (Molau, 1999) that analyses the image streams from ICC7 and ICC9, independently from each other. The ICC8 camera image stream is read into a separate detection software called SpecRec on the computer of ICC7. In case the MetRec detection software of camera ICC7 detects a meteor, a hardwired trigger signal (RS232 serial port) is transferred to the ICC8 detection software. The image stream including the three images acquired before the trigger signal arrived are stored onto a hard disk. The MetRec software stores for each individual frame of each detected meteor event the right ascension and declination of the photometric centre of the meteor and the magnitude. It also stores an estimate of the cloud coverage with one minute accuracy. The computers are synchronised to a network-provided time signal every two minutes. A more detailed description of CILBO setup and its cameras is available in Koschny et al. (2013b).

2.3 System Performance

Since its start of operations in 2012, the cameras ICC7 and ICC8 have individually recorded over 90 000 meteor events, as indicated in Table 2. To apply the wavelength calibration on these events, the calibration routine we have developed requires that both zero-order images recorded by ICC7 and first-order spectra from ICC8 be available simultaneously (further explained in Section 4). About 14 000 were recorded by both systems simultaneously. The distribution of these events per year is listed in the column *Simultaneous Events* of Table 2.

See Koschny et al. (2017) for a more detailed analysis covering 2012 to 2017. The 3D trajectory and heliocentric orbits of these meteoroids were computed using the MOTS (Meteor Orbit and Trajectory Software) code (Koschny and Diaz del Rio, 2002; Koschny et al., 2015b). Column *ICC8 Spectral Events* in Table 2 refer to the identified, full spectra obtained. In this

paper, we focus on the analysis from 2012 to 2017, as afterwards the transmissivity of the grating has been degraded. We have also excluded spectra that are not fully contained in all frames of the meteor event.

3 Radiometric Correction and Background Subtraction

Each detected meteor event results in a number of bitmap (BMP) images files for ICC7 and ICC8, as well as an "information
105 file" for ICC7 which contains measurement results for the meteor. The image files contain the three images acquired before the first detection of the event, as well as three images after the meteor event is lost.

As the CILBO setup has not foreseen a camera door or shutter, a dark current image is only available from the time of the initial setup of the overall system in 2012. A flatfield image is produced synthetically taking the median values for each pixel of an image sequence obtained on a clear night, and then used throughout the years. First, all images, including the pre- and
110 post-images, are radiometrically corrected by dark current subtraction and the flat-field division.

To compensate for acquisitions taken during cloudy conditions or during dawn or dusk, the six radiometrically processed pre-event and post-event images are stacked together into a background image: for each pixel, the median value of the six available pixel is taken.

Each radiometrically processed image in the meteor sequence is then subtracted by this background image. This operation
115 also subtracts the stars from the images and would result in a low background image in case no spectrum is visible. A so-called total image is created by selecting for each pixel location the median pixel value of all images of the meteor sequence obtained so far. The total image provides a summary of the full meteor event and allows to have a quick look on an event and judge the spectrum brightness.

The obtained image sequence as well as the total image, dark current and flatfield, are stored in a single FITS-formatted file,
120 referenced as *level-0 dataset* (see Chapter 9 for a detailed description).

4 Wavelength Determination

Different to other algorithms described so far (Borovicka, 1994a; Dubs and Schlatter, 2015), our algorithm determines the pixel position as a function of wavelength in the ICC8 image, computed from the position in the zero-order image from ICC7. This is done by taking the angular offset between the two cameras into account. During the operational period of the cameras,
125 this angular offset was derived several times from measurements and confirmed to be stable. The basic idea of this step can be best compared to the 2-dimensional diffraction formulae as we know it from the single-slit optical diffraction experiment:

$$\sin \theta = \lambda/d \tag{1}$$

Knowing the wavelength λ and the slit width d , one can compute the angle θ and thus the location of the maxima and minima.

Assuming a Fraunhofer's diffraction at the grating, the light of a star or meteor is considered as parallel entering light rays
130 and its resulting diffraction can be expressed using the 3-dimensional grating formulae as provided in equation (2).

$$\vec{v}^{Lens}(\lambda) = \begin{pmatrix} -x^{Grating} - (n\lambda d) \\ -y^{Grating} \\ \sqrt{1 - (x^{Grating} + (n\lambda d))^2 - (y^{Grating})^2} \end{pmatrix} \quad (2)$$

with:

- $\vec{v}^{Lens}(\lambda)$ represents the direction of the diffracted light in respect of the lens for each wavelength λ ,
 - $(x, y)^{Grating}$ are the coordinates on and in the plane of the grating, at which the light enters
- 135
- n is the grating order which has +1 as nominal value;
 - λ is the wavelength (in meter);
 - d is the groove density (in number of grooves per meter).

With the information from ICC7, especially the right ascension and declination of the meteor, the zero-order, for each individual frame, this diffraction vector $\vec{v}^{Lens}(\lambda)$ for any wavelength λ can be calculated. To derive the (x, y) coordinates at the CCD frame, a sequence of reference frame transformations has to be applied. We further assume that all reference frames are right-handed ones and that the reference frames' z-axes are aligned to each other, in particular the CCD, the optical, and the grating z-axes.

140

As a first step, we have to derive the $(x, y)^{Grating}$ coordinates of equation 2, by applying the following reference frame transformations:

145

$$- \mathcal{F}_{Celestial} \longrightarrow \mathcal{F}_{LocalHorizon}$$

This transformation converts a meteor position (right ascension and declination in J2000, as obtained from ICC7 information) for a given time from the Earth centred celestial frame into an observer centred frame (altitude, hour angle), with the horizon as the fundamental frame, using the python routine *eq2hor*.

150

$$- \mathcal{F}_{LocalHorizon} \longrightarrow \mathcal{F}_{Grating}$$

This transformation converts a meteor position (altitude and hour angle) for a given time from the observer based frame into a grating centered reference frame. This conversion requires the knowledge of the azimuth and elevation of the +x-axis and +y-axis of the grating, respectively. Assuming that it is identical to the optical axis of the complete camera system, it can be computed from the right ascension and declination of the center of the field of view at any given time. The boresight angle, the angle that the z-axis of the grating is tilted, allows for a non-horizontal plate. Unfortunately, this value was not measured at the time of the CILBO installation and we use a rotation value of -11.0 degree as best fit value in the z-axis. The tilt angle describes a rotation of the grating, a rotation of the x-y-plane of $\mathcal{F}_{Grating}$ perpendicular to the +z axis of the grating. If these angles are known, a transformation matrix can be constructed to convert any vector in the horizontal frame into a vector in the grating frame as follows:

155

$$\mathbf{x}^{Grating} = M_{azimuth} \cdot M_{elevation} \cdot M_{boresight} \cdot M_{tilt} \cdot \mathbf{x}^{LocalHorizon} \quad (3)$$

160 – $\mathcal{F}_{Grating} \rightarrow \mathcal{F}_{Lens}^\lambda$ can be determined with equation 2, and produces for each wavelength λ a vector.

From the vector $\overrightarrow{v^{Lens}(\lambda)}$ one could directly transform into the CCD frame and obtain the (x,y) coordinates of the image by normalizing the z-component of $\overrightarrow{v^{Lens}(\lambda)}$ to 1. From the known field-of-view of the camera, one can construct vectors from the CCD center to the field-of-view corners assuming again that the z-component equals to 1. From these relations we can derive the x-position and y-position in the CCD frame of the meteor directly.

165 We follow a different approach, and transform the obtained vectors back in an inverse transformation into $\mathcal{F}_{Celestial}^\lambda$ by applying the inverse matrices of equations 2 and 3. As a result, we obtain the Celestial coordinates for each wavelength. With the knowledge of the plate constant of the camera, these coordinates can be directly transformed into the image (x,y) coordinates. We used the python method `all_world2pix()` of the `astropy.wcs` class. To allow this last transformation, we use the web-service offered by `astrometry.net` (Lang et al., 2010)(<http://nova.astrometry.net>) to obtain a registered image. This registration was
170 done once with an image under good seeing conditions. As the web-service registration also takes the geometric distortions into account, the algorithm does not need to apply any additional distortion correction routines.

The calibration step results for each frame in a list of wavelengths and its corresponding digital value at the computed image position and is stored in a single FITS file labeled as *level-1 dataset* (see section 9 for a detailed description).

It is noted that the accuracy of our algorithm - determined through the correct identification of the (x,y) position of a maxima
175 for a chemical element - was not always satisfactory. As the bright pixels representing the zero-order meteor in ICC7 are spread over many pixels, a centroid algorithm is used in METREC, that did not always correspond to the centre pixel of the meteor as visually observed. The difference was within a few pixels, however the impact on the overall accuracy of the algorithm was too large to neglect. The problem was corrected in a later processing step (see Section 7.2) by adding the wavelength itself as one of the Bayesian parameters.

180 5 Spectral Calibration

5.1 Spectral Response of ICC8

The spectral response curve for ICC8 was derived from images containing the first order spectrum of Vega.

Vega is an A0-type star with a well-known emission spectrum in the visible range. A reference spectrum of Vega was taken from the STIS CALSPEC Archive at https://archive.stsci.edu/hlsps/reference-atlases/cdbs/current_calspec. To obtain an ICC8
185 Vega spectrum, four frames acquired on four consecutive days were selected. Each frame is then radiometrically processed and the wavelengths are derived as provided in section 3 and 4. The final observed Vega spectrum is the median of the four calibrated and atmospheric-corrected spectra. ICC8 spectral response curve is the ratio between the final observed spectrum and the reference spectrum, fitted with a 12-th order polynomial, and normalized to 1, as shown in Figure 3. To validate the

ICC8 spectral response, acquired spectra of Algol, Castor, Deneb, Elnath, and Vega underwent our calibration pipeline and
 190 were compared to the spectra provided in CALSPEC or HyperLeda (<http://leda.univ-lyon1.fr/>).

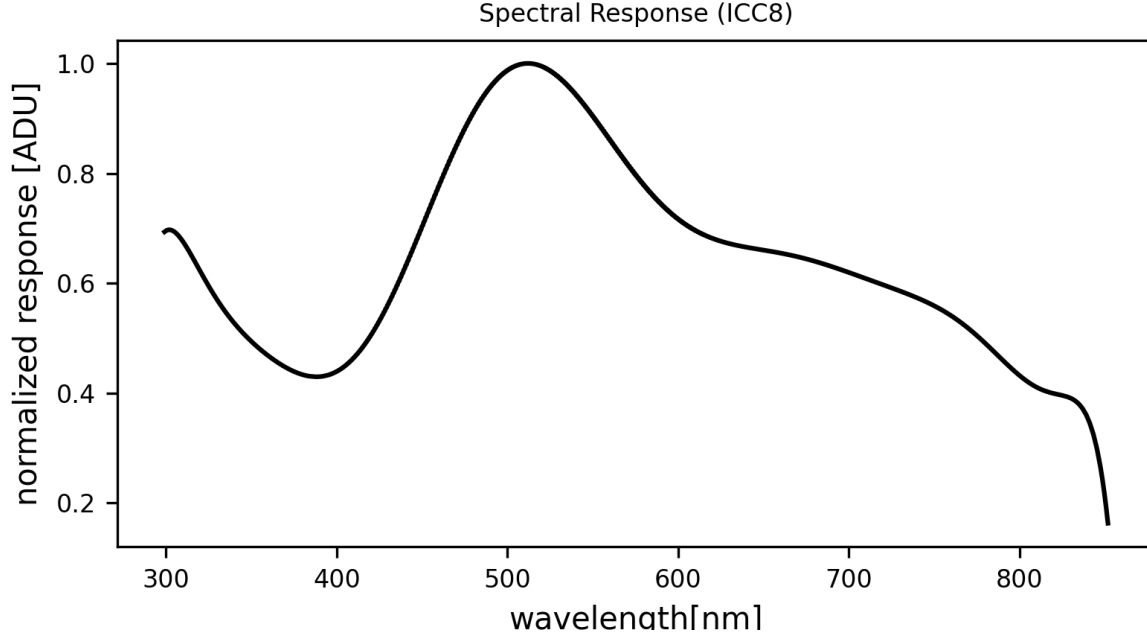


Figure 3. Normalized ICC8 spectral response curve

5.2 Correction of Atmospheric Attenuation

As the light emitted from the ablation process undergoes atmospheric extinction, we apply a correction to the spectral response curves as obtained in Section 5. The scattering and absorption correction is applied to each individual frame and depends on the exact observation geometry, especially the zenith angle of the observed meteor θ_{met} and the optical thickness b_{met} of the
 195 atmosphere. The extinction law can be described as a correction vector (Appenzeller, 2013), as follows:

$$\vec{v}_{corr} = \frac{\vec{F}_{0,met}}{\vec{F}_{met}} = \frac{1}{\exp\left(\frac{-\vec{b}_{met}}{\cos(\theta_{met})}\right)} \quad (4)$$

where \vec{F}_{met} represents the intensity of each feature of the observed meteor spectrum, and $\vec{F}_{0,met}$ the intensities of the true, atmospheric-corrected, spectrum. The atmospheric optical thickness is a coefficient specifying the attenuation of light through the atmosphere; \vec{b}_{met} is a vector varying with wavelength. In case we consider only scattering contributing to the atmospheric
 200 extinction and the aerosols absorption, $\vec{b}_{met} = \vec{b}_{sca}$ is obtained as in Equation (5), with N_{gas} the column number density of gas molecules (obtained using Equation 6), σ_{sca} the scattering cross section of gas molecules (obtained with Equation (7)),

and AOT the contribution of the aerosol optical thickness. The AOT is taken from NASA's AERONET (NASA's AERONET database is found at https://aeronet.gsfc.nasa.gov/new_web/aerosols.html). The file which contained the data used was named "Aerosol Optical Depth (AOD) with Precipitable Water and Angstrom Parameter.) database. The data was recorded by an AERONET sun-photometer in Izana, Tenerife, located at around 1.17 km ground distance from our ICC8 camera. The data is provided at discrete, irregular intervals from 340 nm to 870 nm.

$$\vec{b}_{met} = \vec{b}_{sca} = N_{gas} \cdot \sigma_{sca} + AOT \quad (5)$$

$$N_{gas} = \frac{p_{bottom} - p_{top}}{m_{gas} \cdot g} \quad (6)$$

210

$$\sigma_{sca}(\lambda) = \frac{24\pi^3}{N_L^2} \frac{(n^2 - 1)^2}{(n^2 + 2)^2} \frac{(6 + 3\delta)}{(6 - 7\delta)} \frac{1}{\lambda^4} \approx \frac{C}{\lambda^4} \quad (7)$$

m_{gas} is the air mass (obtained for dry air conditions (28.96 g/mol)) and g the gravitational acceleration (9.806 m/s²), both considered constant through the atmosphere. p_{bottom} and p_{top} are the pressures at the altitudes of the atmosphere corresponding to the begin and end of the meteor ablation. In equation (7), n is the gas refractive index (assumed constant), N_L the Loschmidt's number (2.54743 10²⁵ m⁻³) and δ the gas depolarization constant (0.03 for terrestrial air, ignoring the λ -dependence).

As several of the parameters depend on the line-of-sight between the station ICC8 and the meteor location, thus the meteor altitude, the atmospheric correction is applied to each individual frame of a meteor event. The altitude-varying parameters are computed as follows. g and n are approximated as constants between ICC8 (the troposphere) and the meteor location (the thermosphere).

220

p_{top} is calculated using equation (8):

$$p = p_0 \cdot \left(1 - \frac{L \cdot h}{T_0}\right)^{\left(\frac{g \cdot M}{L \cdot R_0}\right)} \quad (8)$$

where p_0 is the SI standard pressure (101325 Pa), L the temperature lapse rate (9.76 K/km, dry air), T_0 the SI standard temperature (288.16 K), M the molar mass (0.029 kg/mol, dry air), and R_0 the universal gas constant (8.314 J/(mol·K)).

225

A detailed discussion of the assumptions, especially related to the atmospheric values, the improvements obtained, and potential further improvements of the correction using the atmospheric extinction correction can be found in Vicinanza et al. (2021). Figure 4 shows a spectral profile before and after the atmospheric extinction correction was applied.

This calibration step results for each frame of a meteor event in a list of wavelengths and its corresponding spectral calibrated and atmospheric corrected value are stored in a single FITS file labeled as *level-3 dataset* (see section 9 for a detailed description).

230

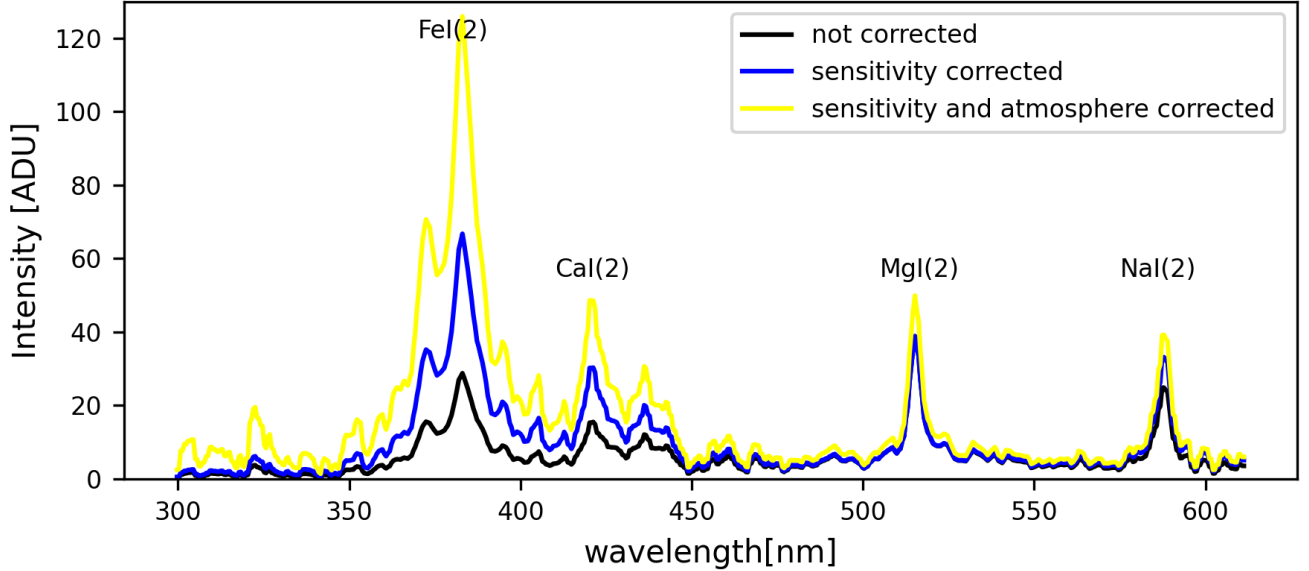


Figure 4. Example of ICC8 spectral profile before (black), after the instrument sensitivity (spectral response) correction (blue), and after the atmospheric extinction correction (yellow).

6 Intensity Calibration

The aim of the intensity calibration is to convert the spectral intensity, measured in CCD pixel counts often expressed as Arbitrary Digital Units (ADU), to a SI Physical units ($\text{W}/\text{m}^2/\text{nm}$). This allows to infer the true and absolute composition of elements in a meteoroid during the extraction of the line intensities of individual chemical elements (as will be described in Section 7). The intensity calibration is done in two steps following Jenniskens (2007): the calculation of the zero-point bias and the estimation of the coefficient of intensity calibration.

The calculation of the zero-point bias involves a photometric calibration. This is performed using the observations of A0V standard stars, simultaneously recorded in the background of meteor observations. We used Vega which has a V-band magnitude m of approximately 0. Knowing the spectral intensity of Vega observed from ICC8, expressed as the sum of ICC8 pixel brightness $\sum F$, the zero-point bias C is obtained using the relation:

$$m = C - 2.5 \log \left(\sum F, \text{ in ADU} \right) \quad (9)$$

where $\sum F$ is Vega's sum of the pixel brightness, and C is the zero-point bias we want to obtain. By applying this step to our set of CILBO observations, a value of 10.81 ± 0.1 was obtained for the zero-point bias. Theoretically, this step should be performed separately for each individual meteor event, using the stars observed in the meteor's background. However, since it

was observed that the zero-point bias remains approximately constant throughout different events, a constant term was applied during our research to the calibration of all events.

The zero-point bias is then used for the estimation of the coefficient of intensity calibration, k , according to the relation below (Jenniskens (2007)):

$$250 \quad k = \frac{3.67 \times 10^{-11} \cdot 10^{-C/2.5}}{EW} \quad (10)$$

where C is the zero-point bias and EW is the equivalent width of the spectral response (measured as the full-width-half-maximum) of the camera (see Fig. 3) and allows to perform a correction for the instrument aperture. Equation (10) is obtained knowing that the zero magnitude A0V standard star Vega has a flux of $3.67 \times 10^{-11} \text{ W m}^{-2} \text{ nm}^{-1}$ at 548.3 nm (V-band). On average, the coefficient k , separately calculated for each event, was around $2 \cdot 10^{-17} \text{ W m}^{-2} \text{ nm}^{-1} / \text{ADU}$. Once this
 255 coefficient is obtained, the calibrated meteor spectral intensity (at each wavelength λ) is obtained from the observed meteor flux F following the relation:

$$F_{\lambda}^{cal} = k \cdot f \cdot \left(\sum F, \text{ in ADU} \right) = k_{corr} \cdot \left(\sum F, \text{ in ADU} \right) \quad (11)$$

F is the average of the flux over 10 binned pixel rows. Since the coefficient k is obtained using Vega star observations and we want to perform the intensity calibration on meteor observations, the correction factor f is needed. This accounts for
 260 the dependence of the intensity calibration coefficient k_{corr} on the exposure time of the star measurement, compared to the exposure time of the meteor measurement:

$$f = \frac{\text{exposure time star}}{\text{exposure time meteor}} \quad (12)$$

The exposure time of a Vega observation is equal to the observation time for the entire meteor event. Since we perform the intensity calibration for each meteor frame (10 binned pixel rows), the exposure time of the meteor is a ratio of the time
 265 delay between consecutive frames. Our cameras have a frame rate of 25 FPS, thus 0.04 s interval between consecutive frames (Koschny et al. (2013b)). The exposure time of the meteor in each frame can thus be obtained as:

$$\text{exposure time meteor} = \frac{0.04 \text{ s}}{\Delta y_{i,i+1}} \cdot \text{number binned pixel rows} \quad (13)$$

where $\Delta y_{i,i+1}$ is the difference in y-coordinate between consecutive MetRec recordings and depends on the meteor speed.

In conclusion, the coefficient of intensity calibration k — used to convert the spectral intensity of meteors spectra from some
 270 Arbitrary Digital Units (ADU) to SI Physical units ($\text{W/m}^2/\text{nm}$) — was considered constant for diverse observations of the same meteor event, while it changed between different meteor events. The change mostly depends on the different exposure times of different meteor events (related to the different meteor speed), the different conditions of atmospheric extinction encountered at different meteor entries, and the optical and camera characteristics (as obtained through the zero-point bias). In our cases, the coefficient k was in the order of $2 \cdot 10^{-17} \text{ W/m}^2/\text{nm}/\text{ADU}$.

To determine the chemical elements and their contribution to a meteor spectral profile, a line-by-line emission simulation has to be executed for each potential chemical atom, molecule, or oxide. The atomic behaviour of each species needs to be modelled, taking into account a number of model input parameters, especially the ablation temperature and the chemical elements number densities. As the selection of slightly different input parameters results in a different spectral profiles that might or might not match a meteor spectral profile from the level-3 datasets (see 9.3), we have to solve an optimization problem. The CILBO calibration pipeline uses the Plasma Radiation Database (PARADE) line-by-line emission simulation tool (Smith, 2006). We use the Bayesian formalism to solve the optimization problem, and the PARADE tool is called from within the Bayesian method, both discussed in the following sections.

7.1 The Plasma Radiation Database

The synthetic spectra are produced by ESA's Plasma Radiation Database (PARADE) tool, originally used to simulate variation of probe entries into planetary atmosphere's (Smith, 2003; Pfeiffer et al., 2003; Liebhart et al., 2012). PARADE calculates the energy state transitions in atoms and molecules and provides the emission coefficient ϵ in radiance $\text{W/m}^3/\text{sr/m}$.

While the number of gaseous elements was originally restricted to the main atmospheric constituents of the atmospheres of Titan, Earth, and Mars, several new species has been added to support our spectral analysis activities for the CILBO acquired spectra. A detailed discussion is given in Loehle et al. (2021) extending the available species to include Na, K, Ti, V, Cr, Mn, Fe, Ca, Ni, Co and Li. The positional information of an emission (or absorption) line is defined by the energy gap between the electron excitation levels as defined by e.g. Herzberg (1950).

$$\Delta E = h\nu = \frac{hc}{\lambda} \quad (14)$$

The energy levels of atoms are exclusively defined by their electron configuration and energy levels. These can be determined from the NIST database (Ralchenko and Kramida, 2020) directly. For molecules, the vibration and rotation of the nuclei are additional parameters to consider. A simple radiation model for diatomic molecules based on a Boltzmann distribution of the vibrational bands and under the assumption of thermal equilibrium, is presented in Equation 15 (Loehle et al., 2021).

$$\frac{N_J}{N} = \frac{hcA_{v,u}}{kT} (2(J-1) + 1) e^{(-A_{v,u}(J-1)(J+1)100 \frac{hc}{kT})} \quad (15)$$

Here h denotes the Planck constant, k the Boltzmann constant, c the vacuum speed of light, $A_{v,u}$ the Einstein coefficient for a spontaneous emission from a lower to a higher state N_J , J the rotational quantum number, and T the temperature.

In addition, we have further extended the PARADE tool by the following molecules CO, CO₂, AlO, CaO, FeO, MgO, NO, and TiO.

To avoid the repetitive execution of PARADE simulations in the upcoming processing step (see Section 7.2), a database is created containing for each species the emission profile over the spectral regime for temperatures in a temperature range from

2000K to 15000K in a 50K granularity. When building up the synthetic emission lines, FeI is processed over the full spectrum, as well as over a limited spectral width that covers explicitly the FeI (15) multiplet response, ranging between 520 to 550 nm. The modelled spectra include the contribution of the Planck background at the individual temperatures, for details see Loehle et al. (2021). In summary, the following atoms, molecules, and ions are available in our database: NaI, MgI, FeI, FeI(15), CaI, 310 SiI, AlI, MnI, CrI, Ar, C₂, CH, CN, CO₂, FeO, CaO, AlO, MgO, O₂, OH, TiO, Na+, Mg+, Fe+, Ca+, Ar+.

7.2 Optimization of the Spectral Fitting using the Bayesian Methodology

The PARADE tool allows to compute the radiative emission of gas species by calculating the line position, its intensity and distribution, i.e. the line profile (Herzberg, 1950; Loehle et al., 2021; Rudawska et al., 2020) for a given temperature and given number density of a selected gas species.

315 Taking the reduced line profiles as obtained after the calibration steps (the data set level-3), a fit to the set of simulated results from the PARADE tool must be found. To solve this *inverse* problem we use the Bayesian treatment of the inference, *the Bayes' theorem*, and apply it to the meteor ablation process.

Having priors is of key importance in the Bayesian framework as priors express our existing knowledge about the parameter space. Parameters for which a lot of knowledge is available are named *informative priors* in the Bayesian framework. They 320 are updated by the algorithm based on new data provided. In our case, we have three *informative priors*, all being input parameters to the PARADE simulation. First, the total number of atoms or molecules of a gaseous species directly relating to the maximum values of the simulated line profiles. We consider this number to be uniformly distributed. The temperature of a meteor ablation process is an *informative prior* and we assume a uniform distribution. Following the identification of two distinct thermal components in the meteor ablation by Jenniskens (2007), we take two distinct temperature components, T_1 325 and T_2 , as *informative priors*.

Uninformative or *ignorance priors* are very diffuse and they do not constrain the parameters. These are used when we do not have a lot of knowledge about the parameter beforehand and are not used within the PARADE simulations. We use three *uninformative priors* in our framework.

- The PARADE tool takes into account several line broadening effects within its simulation like the Van de Waals, or 330 natural or Stark broadening. As the errors associated with these models are not yet fully quantified, we have introduced the standard deviation of the instrumental broadening, σ , as an *uninformative prior* and consider its distribution function as uniform.
- We have reported in 5 an uncertainty in the position measurement of the meteor center that we are not able to characterize further and have therefore introduced as *uninformative prior* the uncertainty along the wavelength axis, $\Delta\lambda$, of the 335 measured line profiles. Also for this *uninformative prior* we assume a Gaussian distribution.
- Moreover, the line profile itself constitutes a level of signal noise, that propagates through the algorithms (as described earlier), and is difficult to characterise. We thus introduce another *uninformative prior*, the line profile background b , assuming a Gaussian distribution.

Table 3. Overview of the parameters of our model, the choice of prior, and initial settings.

| parameter | description | parameter type | prior | initial setting |
|----------------------|--|----------------------|------------------|-------------------|
| $\log N_X$ | Logarithm of the total number of atoms or molecules of species X | <i>informative</i> | $U(-5, 35)$ | |
| T_1 [K] | Temperature of the main spectrum | <i>informative</i> | $U(3000, 5000)$ | 4500 |
| T_2 [K] | Temperature of the second spectrum | <i>informative</i> | $U(4000, 15000)$ | 10 000 |
| σ [nm] | Standard deviation of the instrumental broadening | <i>uninformative</i> | $U(0, 5)$ | 2 |
| $\Delta\lambda$ [nm] | Shift along the wavelength axis | <i>uninformative</i> | $N(-5, 5)$ | 0 |
| b | Background count rate | <i>uninformative</i> | $b^{-1/2}$ | min(line profile) |
| R [m] | Radius of the meteor (shaped as isotropic sphere) | <i>uninformative</i> | $U(0.1, 10)$ | 1 |

Finally, we need to convert the modelled synthetic spectra in irradiance (W/m³/sr/nm) into radiance (W/m²/nm). This is done by performing a solid angle conversion assuming the meteor to have the shape of an isotropic sphere (Jenniskens (2007)). We introduce a final *uninformative prior*, the size of the ablating body, the meteor, in the direction of flight R , assuming a uniform distribution. From R we derive the luminous area of the radiating body as $\pi * R^2$.

Table 3 lists all priors and their initial settings.

The Bayesian treatment of the inference, *the Bayes' theorem* can be written as

$$P(\theta|Y) = \frac{\mathcal{L}(Y|\theta)\pi(\theta)}{\pi(Y)}. \quad (16)$$

$P(\theta|Y)$ denotes the probability of a model applied over a parameter space θ , in our case the temperature, the instrumental line broadening, the uncertainty in the wavelength, and the background count rate, given a set data samples $Y = (y_0, y_1, \dots, y_N)$. y_i denotes line intensities simulated for the individual species. In literature, $P(\theta|Y)$ is typically referred to as the *posterior*. $\pi(\theta)$ are the probabilities of the parameters, the *prior*. Finally, $\pi(Y)$, typically referred to as the *evidence*, are the probabilities of the simulated line profiles.

$\mathcal{L}(Y|\theta)$, the *likelihood*, is the product of the probability of the individual data points:

$$\mathcal{L}(Y|\theta) = \prod_i^N P(y_i|\theta) \quad (17)$$

given an independent set of data points $Y = (y_0, y_1, \dots, y_N)$ sampled over $X = (x_0, x_1, \dots, x_N)$.

Assume we have a parameterized model $f(x|\theta)$ which models the data Y for given parameters θ and explanatory variable X , in our case the wavelength. With this model we can then calculate the probability of generating an observed data point

$P(y|\theta)$, also known as the *likelihood* $\mathcal{L}(y|\theta)$. If we have an independent set of data points $Y = (y_0, y_1, \dots, y_N)$ sampled over all wavelength $X = (x_0, x_1, \dots, x_N)$, the total likelihood is the product of the probability of the individual data points.

360 As the measured line profiles from the gaseous species are derived from CCD images, thus photon counts, the likelihood of the probability distribution line profiles over wavelength are given by a Poisson distribution.

$$\mathcal{L}(Y|\theta) = \prod_i^N \frac{f(x_i|\theta)^{y_i} \exp(-f(x_i|\theta))}{y_i!} \quad (18)$$

Instead of using the likelihood as in equation (18), it is common to work with the log-likelihood, as that reduces the product to a sum over the data points. In the Poisson case, the negative log-likelihood is given by:

$$365 \quad -\ln \mathcal{L}(Y|\theta) = \sum_i -y_i \ln(f(x_i|\theta)) + \sum_i f(x_i|\theta) + \sum_i \ln(y_i!) \quad (19)$$

Before we can start the Bayesian framework, an *initial guess* of the synthetic spectrum is computed, based on the values in Table 3. As we study the optically thin case (optical depth $\tau \ll 1$) and use discrete temperature values, the final, synthetic spectrum is then a linear combination of the individual emission spectra of each species as described in equation (20).

$$F_\nu^{\text{source}}(T) = \sum_i N_i j_{\nu,i}(T) \quad (20)$$

370 where F_ν^{source} is the flux vector of the complete source spectrum, i.e. the sum of the spectra of all species "i" at the source, N_i the number density of each species, and $j_{\nu,i}$ the temperature-dependent emission coefficient of element i. The elements' emission coefficients are retrieved from the PARADE database (introduced in Section 7.1). The flux vector F_ν comes from the meteor observations. The only unknowns of the equation are the number densities N_i .

The estimation of the number densities of the meteor's radiating elements, is articulated in three sequential steps: a linear regression retrieval, a nonlinear least-squares initial solution, and the final Markov Chain Monte Carlo (MCMC) parameter estimation.

For each species and each discrete temperature in our emission database (described in Section 7.1), the obtained spectral profile is further modelled into a set of synthetic spectra. These are obtained through different combinations of the parameters in Table 3, left free to vary within defined boundaries (*Prior* in Table 3). A linear solution of the parameters in Table 3 is then retrieved, estimating the Moore-Penrose pseudo-inverse of the matrix having on its rows the species' synthetic spectra obtained at each combination. By applying a linear regression, considering the ICC8 observed meteor spectrum as the dependent variable, a first estimate of the number density of all the species considered is obtained.

Using these linear estimates as first guess, a nonlinear least-squares approach is used to obtain an even more accurate estimation of the number densities' initial solution. This provides the estimate of all the unknown parameters in Table 3, whose combination generates a complete synthetic meteor which best fits the ICC8 observed meteor spectrum. The nonlinear least-squares solution for the number densities, and other parameters, is determined using the Levenberg-Marquardt algorithm. Our approach is very similar to (Benneke and Seager, 2012), where Bayesian inference is used to retrieve and constrain the

composition of exoplanet atmospheres from their transit spectra. These best-fit least-squares estimates are however only an initial solution; thus do not coincide with the final best-fit solution obtained at the end of the routine, after the Markov Chain Monte Carlo (MCMC).

The least-squares parameter estimates are used as initial guesses for the successive MCMC. Using the MCMC sampling we estimate the posterior distribution of the parameters of the spectral model. The MCMC sampler approximate the posterior distribution by generating samples with a probability that is proportional to the posterior:

$$n(\theta)d\theta \propto P(\theta|Y)d\theta, \quad (21)$$

where $n(\theta)d\theta$ is the number of samples between θ and $\theta + d\theta$. In MCMC methods we generate so-called Markov Chains which follow this distribution. A Markov Chain is a random process which obeys the Markov property that successive data point is only based on the most recent data point.

$$P(\theta_i|\theta_{i-1} \dots \theta_{i-N}) = P(\theta_i|\theta_{i-1}). \quad (22)$$

We thus obtain not only a point estimate of the chemical composition of the meteor but an estimate of the full probability distribution, giving a constraint on the range of abundances which could describe the meteor. During the MCMC, for each meteor event 1000 iterations are run. Each iteration models a different synthetic spectrum using parameters which are sampled around the nonlinear least-squares solution via MCMC affine-invariance sampling. We use the *emcee* python package (Foreman-Mackey et al., 2013, 2019) that implements the affine-invariant ensemble sampler by Goodman and Weare (2010). The algorithm performed well under all linear transformations and is insensitive to covariances among parameters. The complete synthetic spectrum which best fits the ICC8 observed spectrum is inferred using Bayesian inference: the best-fit parameters represent those for which the posterior has highest value. Specifically, the inference returns the combination of parameters for which the modelled (synthetic) spectra best fit the observed spectra (data).

8 Spectral Calibration discussed on one meteor event

This section guides through the individual processing steps and intermediate results, based the meteor event 20131214T041302. The meteor presented was classified by METREC to belong to the Geminid shower and was observed in December 2013. The meteor itself as well as its spectral signature were detected in 24 individual frames in cameras ICC7 and ICC8 respectively. The maximum apparent magnitude was -1.7.

The level-1 FITS file contains the individual frames, as well as the total image (shown in Figure 5).

In the next processing step, the (x,y) position for each wavelength is determined frame by frame resulting in an line plot representing the meteor spectrum intensity. The profile is further spectrally calibrated and corrected for atmospheric effects resulting in a *level-2A* FITS file. The *level-2B* FITS file contains the final calibration product, after the intensity calibration is applied, in radiance ($\frac{W}{m^2nm}$). The un-processed and calibrated profile of the brightest frame, frame 20, is shown in Figure 6.

The 1000 MCMC iterations of the ablation processes as part of the Bayesian interference algorithms are based on the priors and initial settings as given in Table 3 (see Section 7.2). In our setup - thus also applicable for this example - the initial settings



Figure 5. Total image (max pixel value over all frames) of event 20131214T041302 as observed by camera ICC8.

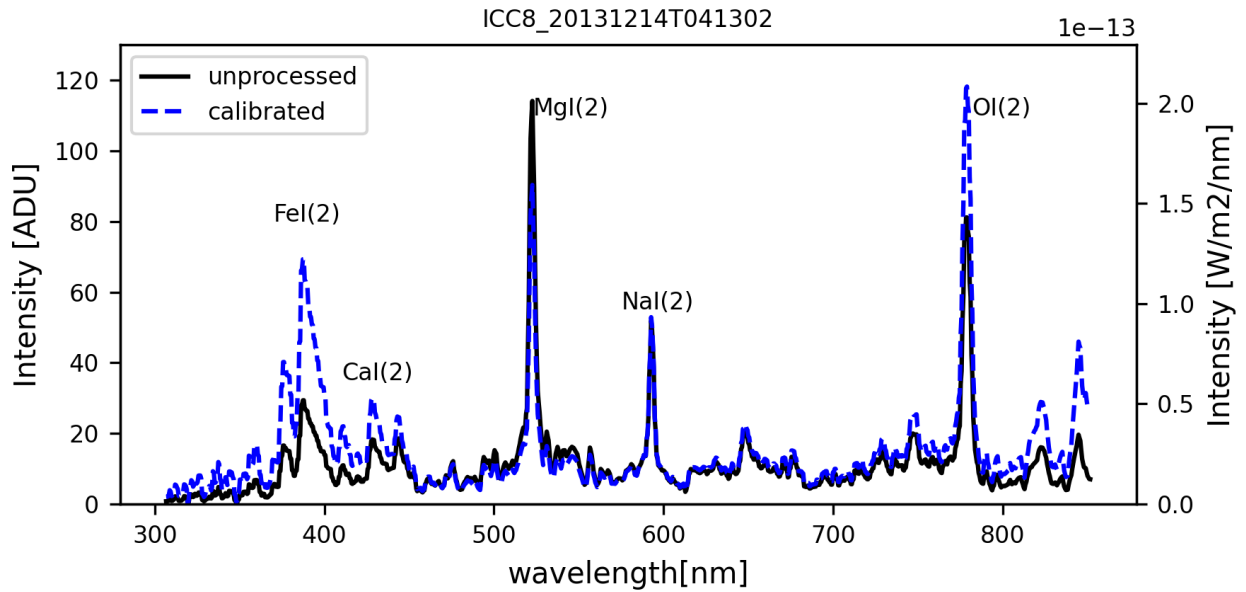


Figure 6. Un-processed (black line) and calibrated (blue dashed) profile plot of frame 20 (20131214T041302).

420 used for the chemical elements are computed by a leased-square fitting algorithm and the resulting values are given in Table 4. The selection of chemical elements, the main temperature, and the secondary temperature (see Section 7.2) proofed stable through the processing of all meteor events. In the future, we might apply a different, larger selection of elements, i.e. when processing meteor events of a dedicated meteor shower.

Table 4. Initial settings for elements and final results obtained. The number density is given in cm^{-3} .

| element | main/secondary | number density (initial guess) | number density (result) |
|---------|----------------|-----------------------------------|----------------------------|
| Fe | main | 1.1×10^7 | 7.97×10^7 |
| Na | main | 3.9×10^4 | 3.18×10^5 |
| Mg | main | 1.35×10^8 | 8.14×10^8 |
| Si | main | 2.57×10^{10} | 1.74×10^{10} |
| Ca | main | 1×10^{-5} | 1.50×10^5 |
| Cr | main | 3.11×10^6 | 9.99×10^5 |
| Ti | main | 2.3×10^6 | 1.58×10^{-4} |
| K | main | 1×10^{-5} | 9.36×10^7 |
| CaO | main | 1×10^{-5} | 1.85×10^{-2} |
| FeO | main | 1×10^{-5} | 5.57×10^7 |
| N2 | main | 2.16×10^{15} | 2.26×10^{15} |
| Ca+ | secondary | 5.58×10^{13} | 4.30×10^{-6} |
| Fe+ | secondary | 1×10^{-5} | 6.97×10^{-6} |
| Mg+ | secondary | 4.95×10^7 | 1.83×10^7 |
| O | secondary | 3.82×10^9 | 1.38×10^{10} |
| N | secondary | 4.13×10^9 | 7.57×10^9 |

After the Bayesian interference algorithm and MCMC run have finished its simulations and the best fit is available, a check
 425 on the convergence of all parameters used in the simulation is needed. This is done by the visual analysis of the so called
 corner plot that is produced by the data pipeline for each meteor event. The corner plot, see Figure 7, (Foreman-Mackey, 2016)
 visualizes the posterior probability distribution of the parameters in diagonals, and the covariances between the parameters of
 the MonteCarlo iterations on the non-diagonals. The distribution of most parameters indicate a Gaussian distribution around
 a best estimate. A clear peak is visible for MgI, but two side maxima are visible. This might indicate either a higher level of
 430 noise, or an interference with another chemical element. From Fig. 10, we could argue that CrI could interfere with MgI.

This validation step is currently the only manual step needed in the calibration pipeline. In case a parameter is not converging,
 the parameter needs to be taken out of the simulation and a rerun of the simulation is needed:

- The two temperature regimes result in temperatures of 4000K and 9000K. The variations in the chain plots are marginal
 and we consider the two temperatures as an important result of our analysis.
- 435 – The chemical elements Fe, Na, Mg, Si, Cr, Ti, K, CaO, FeO, N2, Ca+, Fe+, MG+, O and N converge well.
- The parameters background, wavelength shift, and radius_sphere are also contained in the corner plots (however not
 shown in Fig. 7). The background is a proxy for the noise level in the spectral profiles, the wavelength shift an indicator

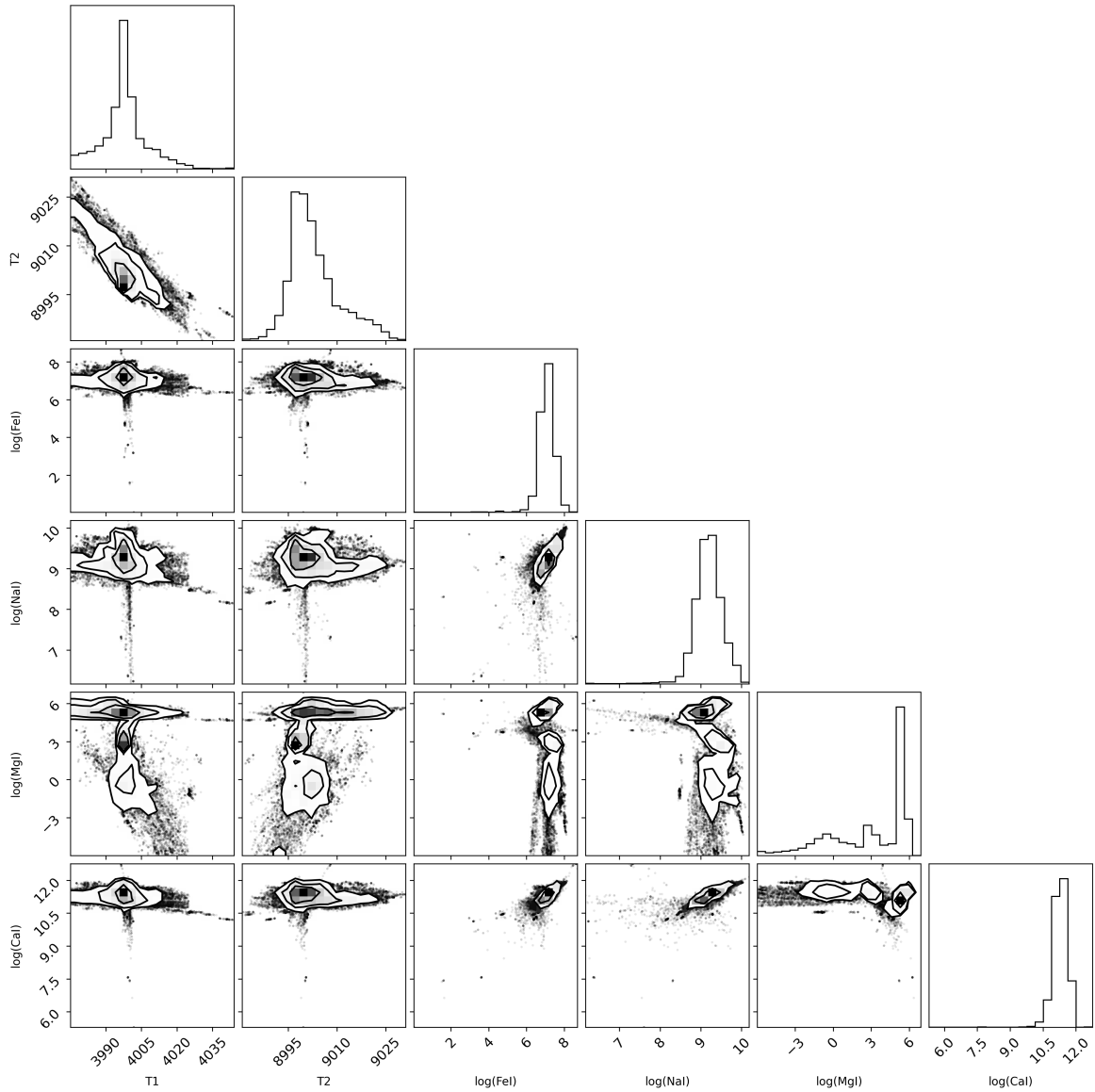


Figure 7. Example of a corner plot, showing the posterior distribution on the diagonals and co-variances of a few, selected parameters in the non-diagonals.

for an additional correction of the wavelength to achieve a good result (in the presented case less than 2 pixels), and `radius_sphere` is the radius of the meteor's luminous area. According to Jenniskens (2007), the meteor is considered as an isotropic sphere, i.e. the radiating area perpendicular to the observer has the same value across all directions of the observer, thus the luminous area equals $\pi \cdot \text{radius_sphere}^2$.

At the end of our event analysis, the data allow the comparison of the observed spectrum to the simulated spectra obtained for the total images and the brightest frame. Figure 8 shows the obtained plots demonstrating the fitting algorithm. Most maxima in the observed spectrum are well fitted. Also the broad bands are fitted well, some overshooting is observed however between 445 550-650nm. The intensity of the individual frame is given on the right yaxis and is of cause less intense than in the total image. The reader shall note that the red line in Figure 8 represents the calibrated spectra in $\frac{W}{m^2nm}$ of the brightest frame and is thus about much smaller than the corresponding black line that represents the energy of the overall meteor event (thus of all the frames).

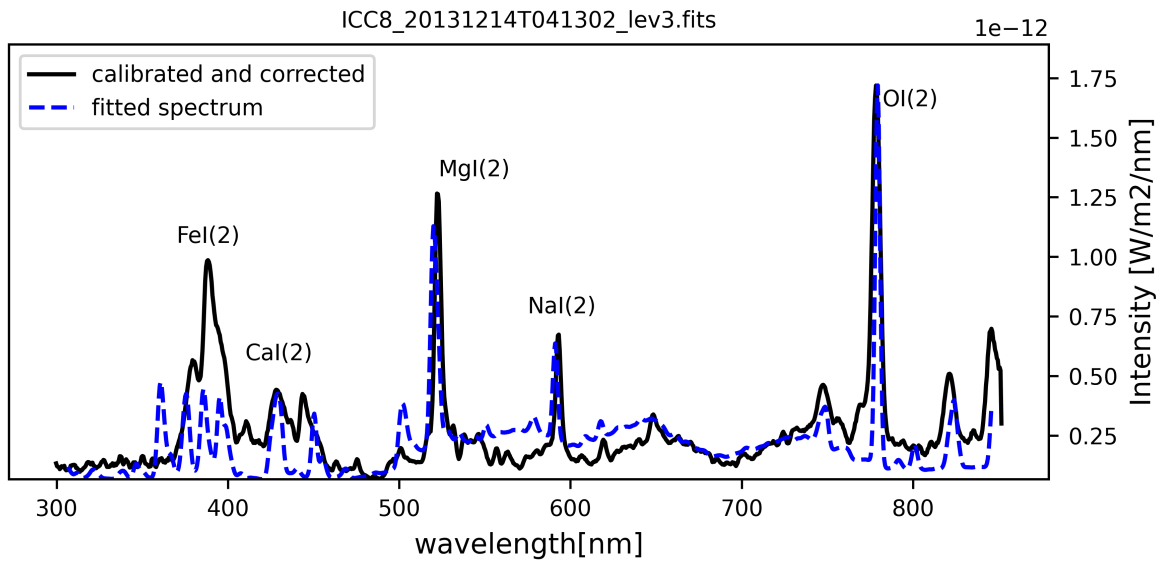


Figure 8. Calibrated spectrum (black line) and fitted spectrum (blue) of total image of event 20131214T041302

Table 4 contains the resulting number densities in the right column, that can be interpreted in the following way:

- 450 – From the meteoric elements, the highest number density is obtained for Si.
- The Na content is relatively small, especially in comparison to the Fe and Mg. As the sodium is a direct indicator of the fluffiness of the meteoroid and thus it's parent body (Abe et al., 2020), this is an indication that the meteoroid might be composed of stronger material without small grains. Our observation confirms earlier studies from e.g. Abe et al. (2020) and Vojáček et al. (2019).
- 455 – Borovička (2010) and Abe et al. (2020) provided ratios of Na/Mg of 0.023 and 0.067 respectively. The value we obtain for the event discussed is 0.0003, and deviates thus a lot.
- Borovička (2010) and Abe et al. (2020) provided ratios of Fe/Mg of 0.32 and 0.3 respectively. The value we obtain is 0.09, a factor of three smaller. Borovička (2010) and Abe et al. (2020) mention however that the values of individual

- 460 meteor events differ largely, by a factor of 2 for Fe/Mg and a factor of more than 10 for Na/Mg. Further investigations are needed to explain the large difference of the CILBO derived ratios to the ones provided in the cited literature.
- Mg/Si and K/Si ratios of 0.046 and 0.005 respectively are in the ranges of the COSIMA instrument on-board of Rosetta (Rubin et al., 2020).
 - The Na/Si ratio of 1.8×10^{-5} is however much smaller than the range given for COSIMA, that is 0.02 to 0.2 (Bardyn et al., 2017).
 - 465 – The Ca/Si ratio of 8.6×10^{-6} is also much smaller than the range given for COSIMA. It must be noted that the COSIMA instrument analyzed the bulk refractory material, which might explain some of the different ratios obtained. Madiedo et al. (2013) states that Ca might not fully vaporize during the ablation which might also explain the low Ca/Si ratio.
 - Cr is observed with high abundance, i.e. Cr/Na = 3.1 and Cr/Ca = 6.6. Chromium measurements were reported earlier by Russell et al. (1956) and lately by Matlovič et al. (2020). The measurements of Matlovič et al. (2020) were obtained from
470 laboratory measurements on meteorite samples and the high Cr value was attributed to the high values of daubreelite (FeCr₂S₄) and lower values of enstatite (MgSi₃O).
 - No Ca and Fe ions are detected in the T=9000K component. It is thus more surprising that the Mg ion number density is relatively large. Mg ions were reported back in Etheridge and Russell (1968). The observations discussed in Jenniskens et al. (2002) indicate that Ca, Fe, and Mg ions are a result of the hot T=10000K component, one would thus expect to
475 find all three ionisation's back. The detailed interpretation of these observations need first to be confirmed by further detailed analysis of other events and supplemented by a better interpretation of the chemical ablation physics.

9 Available Data Sets

Table 5 summarizes the data processing levels used in the CILBO spectral calibration pipeline and in the archive.

480 As the processing is very intensive in respect of time and computing resources, the synthetic spectrum was computed for the total image of each event. This is reflected in the sub-directories and in the names of the FITS structures. The data processing levels level-1 to level-3 are made publicly available via the Guest Archive Facility of ESA's Planetary Science Archive (Besse et al., 2018). All data products are stored in the FITS format (Pence et al., 2010). Level-0 represent the raw, unmodified data, level-1 data the radiometrically calibrated images, level-2 data represent the spectral profiles after radiometric, camera spectral sensitivity, and altitude-dependant atmospheric extinction corrections have been applied. Also, the response to the intensity
485 calibration correction is part of the level-2 data product. The level-3 data contain the derived parameters obtained from the Bayesian framework and MCMC processing: the number densities of the chemical elements, several ablation parameters, and the fitted spectra. Level-3 data are also accompanied by browse images in PNG format.

Table 5. Name, definition and format of the different levels of data within the MRG dataset.

| Level | Definition | Data Format |
|----------|---|------------------------|
| Level-0 | Raw data acquired by cameras at CILBO. No processing. | BMP (INF, LOG, SNF) |
| Level-1 | Data after radiometric (dark current, flat-field, background subtraction) and wavelength calibration of Level 0 BMPs. | FITS |
| Level-2a | Data after spectral calibration of Level 1 spectra. Correction for ICC8 sensitivity and altitude-dependent atmospheric extinction. | FITS |
| Level-2b | Data after intensity calibration of Level 2-A spectra. | FITS |
| Level-3 | Reduced data after MCMC Bayesian inference: chemical elements number density, ablation parameters (T , σ , b , $\Delta\lambda$) and spectra. | FITS, PNG |

9.1 Level-1 Data

The level-1 fits files are radiometrically calibrated, thus dark current subtraction and a flatfield multiplication correction have been applied. The file names are formatted as e.g. *ICC8_20131214T041392_lev1.fits*, combining all information of one particular meteor event into a single file. The primary header provides information on the observation, the camera, and the meteor. The primary data is the total image of the event, thus each pixel represents the maximum pixel value of all frames at this position. The total image allows to obtain a quick indication on the brightness, completeness, and quality of the images available. Keyword-Value pairs in the FITS header represent information of the observation (date, time, observer, location), camera details (name, focal length, manufacturer), or the meteor event itself (brightness, meteor shower identification). Each FITS data product has 4 extensions, each being a binary table. The individual tables are structured in a similar way starting with wavelength information, information on each frame, and finally the information of the total image:

- *ICC8FRAMESINFO*, contains for each frame in the meteor event information on the frame number, the julian date, right ascension and declination in degrees (of the 0-order location obtained from ICC7), the apparent magnitude, the measured signal-to-noise ratio, a wavelength error, the number of CCD rows binned together, the distance between the camera and the meteor, the height of the meteor above ground, and the intensity calibration coefficient. In case, a parameter can not be calculated the 'nan'-value is used, which is e.g. the case when there are no double station observations available and the *height* can not be computed.
- the algorithm has computed based on the 0-order information available from ICC7, the location (x and y position in frame) and the corresponding wavelength for each pixel coordinate. The pixel values of these (x,y) positions are read and combined into an array, or simply profile:
- *ICC8PROFILES*, contains for each frame the derived profile based on the 0-order information

– *ICC8WAVELENGTH*, contains for each frame and for each element in the profile the corresponding wavelength. The wavelength are provided in meters.

510 – *ICC8SENSITIVITY*, contains the normalized instrument sensitivity curve. See Section 5 for further information.

9.2 Level-2 Data

The level-2 fits profiles are corrected for the spectral response of the camera (using the *ICC8SENSITIVITY* information) and corrected for the altitude-dependent atmospheric correction (see Section 5). The result of these corrections is stored as level-2a. The result of the intensity calibration of the level-2a profiles is stored as level-2b profiles. Whereas level-2a data is dimensionless, level-2b data are provided in $\frac{W}{m^2nm}$:

– *ICC8FRAMESINFO* is identical to level1.

– *ICC8LEVEL1* is identical to *ICC8PROFILES* from level-1.

– *ICC8LEVEL2a*, identical structure as in *ICC8LEVEL1*; the camera spectral calibration is applied to *ICC8LEVEL1* profiles using the first array in the *ICC8SPECTRALCAL* extension as calibration curves.

520 – *ICC8LEVEL2b*, identical structure as in *ICC8LEVEL1*; the intensity (absolute) calibration is applied to *ICC8LEVEL2b* profiles.

– *ICC8SPECTRALCAL*, contains the *ICC8* spectral calibration curve followed by the atmospheric correction factors per wavelength for each frame.

9.3 Level-3 Data

525 The level-3 fits products contain the simulation results of the Bayesian method applied to the level-2 data products based on the *PARADE*-based database. The primary header repeats the general information on the meteor event (date, observation information, camera properties, and meteor shower information), a copy from the level-1 and level-2 data products. The two extension tables contain the gas species information for each species and considered frame:

– *TOT_IMAGE_BESTFIT*, contain for each chemical element analyzed with the Bayesian framework:

530 – *SPEC_TYPE* that is either *main* or *second*,

– *NUM_DENSITY* of floating type number in scientific notation. Unit is m^{-3} ,

– information on the temperature regime is given in the first two rows as two temperature regimes were analyzed,

– the Gaussian broadening, the background noise, the wavelength shift applied, and the spherical radius are independent of the elements and provided in the first row only.

- *TOT_IMAGE_SPECTRA*, contains four arrays representing the wavelength, the observed spectral profile, the synthetic spectral profile, as well as the spectral response curve used. From these arrays the spectral profile plots can be re-generated.

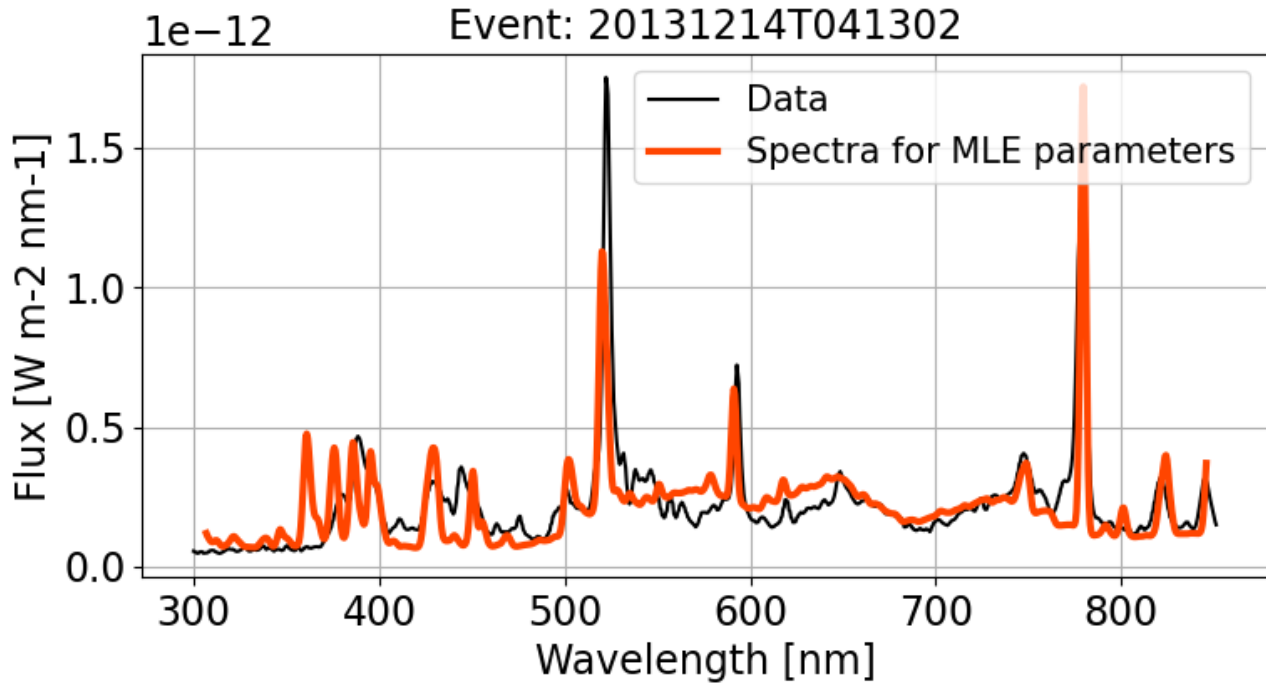


Figure 9. Intensity profile of acquired spectrum (black) and synthetic spectrum (red) resulting from the Bayesian method as retrieved from the level-3 fits file.

For validation purposes the archive contains a subdirectory named 'plots', containing for each meteor event 3 different images in PNG format:

- *eventname_lev3_fit.png*, a plot of the observed spectrum overlaid with the synthetic spectrum, see Fig. 9.
- *eventname_lev3_elementsfit.png*, contains two plots of the observed spectrum, with the synthetic spectra of each chemical element overlaid, see Fig. 10.
- *eventname_lev3_chain.png*, contains the MCMC chain results from each chemical element used in the PARADE simulation, see Section 7.1 and Fig. 7.

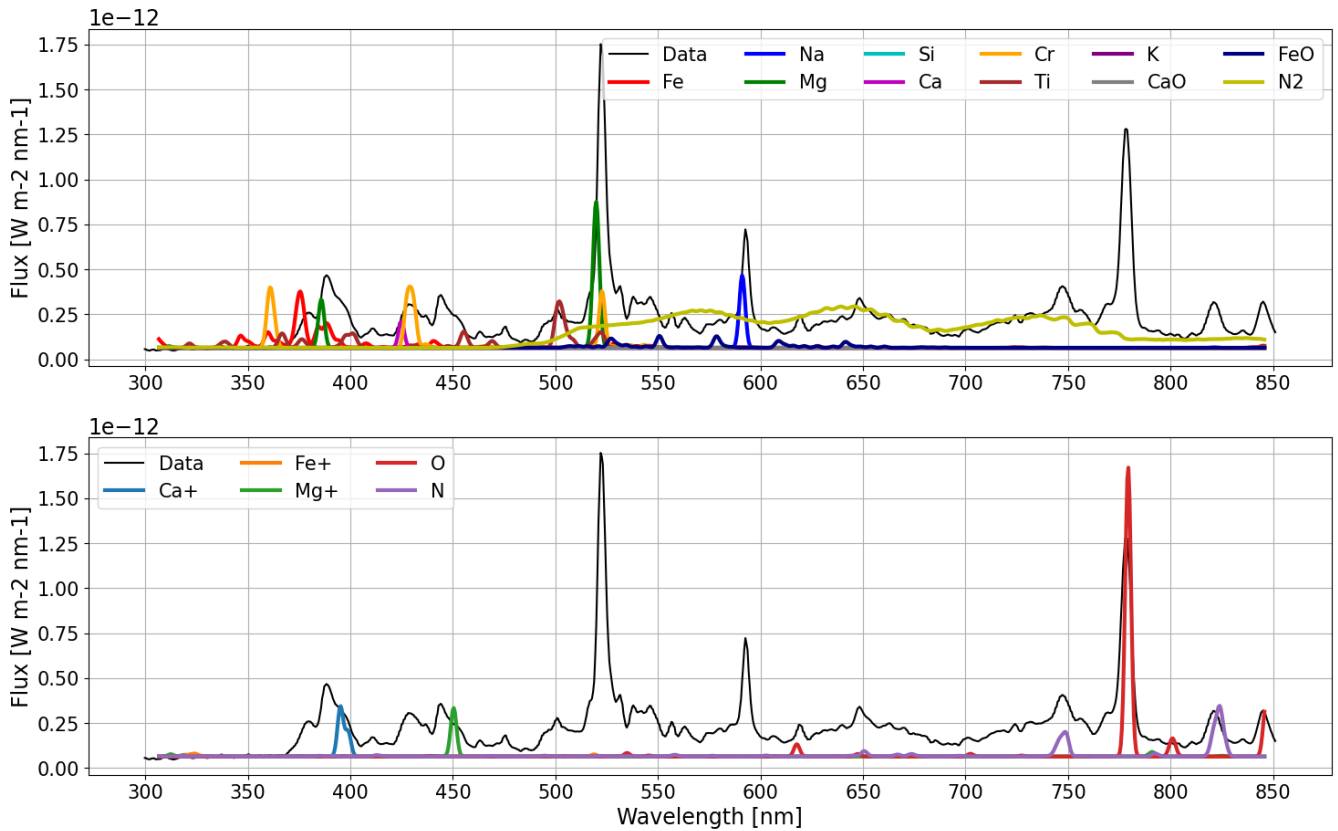


Figure 10. Same as Fig. 9, with top plot showing the synthetic spectra of all chemical elements analyzed for the meteor event for the lower temperature component; lower plot showing the synthetic spectra of all chemical elements analyzed for the meteor event for the higher temperature component. From Fig. 7 one can find that the lower and higher temperature components resulting from the Bayesian method was 4000K and 9000K respectively.

545 10 Summary

We present an algorithm to process meteor events acquired using a camera system with a spectral grating attached to it from its raw format into quantitative chemical information. The algorithm is based on the principle that the location of a specific diffracted wavelength in 1-order can be directly derived from the knowledge of the 0-order position of the meteor. In our setup, we obtain the 0-order information from an image intensified camera, that is mounted with an offset angle to another intensified camera with a transmission grating mounted on-top. The presented algorithm includes the radiometric calibration of the images, the determination of the location of the 1-order information for each wavelength, the extraction of the meteor event spectral profile, and its spectral calibration. The spectrum derived is further corrected for atmospheric effects that take place between the observer and the location of the meteor ablation at the different heights during the event. In the next step, a Bayesian approach is used to map a simulated spectrum against the reduced spectrum obtained by our algorithm. To simulate the ablation we use

555 the PARADE tool that was extended to allow the simulation for most meteoric and atmospheric atoms, di-atomic molecules,
ions, oxides, and a few complex molecules. As pre-knowledge to the Bayesian framework we use the assumption of two main
temperature regimes during the ablation, and the typical chemical elements of meteors and their respective line intensities. After
running typically 1000 Markov-Chain Monte-Carlo iterations, we obtain the simulated spectrum as overall line intensities, but
560 also obtain the line intensities of each chemical element. In a last processing step, the line intensities are calibrated itself,
resulting in the number densities of each chemical element.

Several hundreds of meteor events have been observed by the CILBO observatory in the past decade and we provide full
access to the data in its raw and intermediate calibrated data processing levels. The data is stored using the FITS Standard, and
an overview to the keyword-value pairs in the FITS header, as well as a description of the extended binary arrays using in the
FITS extensions is provided.

565 A discussion of one meteor event, its processing chain, and resulting spectral information is given.

The presented algorithm works autonomous - that means without user interaction. The processing time is however large and
even when using a multi-processor, multi-core system, we have not yet computed all individual frames of all meteor events.
Instead, we have processed for each meteor event the information obtained from the total image as well as from the brightest
frame. In the data set published, we share the data representing the total image.

570 All events contained in the data set has been checked for the convergence of the Bayesian parameters as result of the MCMC
iterations. The list of chemical elements used in the Bayesian approach was not extensive, and in the processing so far, we only
checked for the typical chemical elements also reported by other observers in the past. It is our goal to reprocess all the data
and use more chemical elements that PARADE is currently able to simulate. Such a step, however, needs a very careful study
of the convergence of the chemical elements - which is still a manual step and thus requiring dedicated efforts.

575 **Acknowledgement**

The work presented in this manuscript is the result of efforts over a 10-year period that was executed on a continuous, however
time-limited basis. Many students supported parts of this activity and each of them contributed to this final result presented. All
of these efforts have been either funded by the Science Faculty of ESA's Science Directorate or through studentships provided
for by ESA. Special thanks go to Ms C. Molijn, Ms N. Bartholomae, Mr. K. Ravensberg, Mr. I. Uarte, and Mr. J. Lightfoot. The
580 contributions from Mr. J. Diaz del Rio, Mr. R. Landman, and Mr. L. Maraffa were highly valuable and appreciated. We would
also like to thanks Prof. W. van der Wals and Prof. D. Stam for their important advice on atmospheric physics and co-lead of
students. We would like to thank the reviewers for the critical, constructive review which did lead to many improvements of
the manuscript.

Data availability. The meteor spectra data of the CILBO observatory are freely available at the Guest Archive Facility of ESA/ESAC. DOI:
585 Zender (2023)

Author contributions. The activities reported in this manuscript were led and coordinated by JJZ, DVK and RR. Major contributions in the software development were done by SV and RL. SL did lead the efforts in the extension of the PARADE simulator, and LM for his advice on ablation physics and SL on the implementation of oxides and other chemical elements into the PARADE database. HS for his continuous software support and the installation of the CILBO computing system. DS for the advice on the correction of the atmospheric effects.

590 *Competing interests.* The contact author has declared that neither they nor their co-authors have any competing interests.

References

- Abe, S., Ogawa, T., Maeda, K., and Arai, T.: Sodium variation in Geminid meteoroids from (3200) Phaethon, *Planet. Space Sci.*, 194, 105040, <https://doi.org/10.1016/j.pss.2020.105040>, 2020.
- Altwegg, K., Balsiger, H., Hänni, N., Rubin, M., Schuhmann, M., Schroeder, I., Sémon, T., Wampfler, S., Berthelier, J.-J., Briois, C., Combi, M., Gombosi, T. I., Cottin, H., De Keyser, J., Dhooghe, F., Fiethe, B., and Fuselier, S. A.: Evidence of ammonium salts in comet 67P as explanation for the nitrogen depletion in cometary comae, *Nature Astronomy*, 4, 533–540, <https://doi.org/10.1038/s41550-019-0991-9>, 2020.
- Appenzeller, I.: *Introduction to Astronomical Spectroscopy*, Cambridge University Press, 2013.
- Bardyn, A., Baklouti, D., Cottin, H., Fray, N., Briois, C., Paquette, J., Stenzel, O., Engrand, C., Fischer, H., Hornung, K., Isnard, R., Langevin, Y., Lehto, H., Le Roy, L., Ligier, N., Merouane, S., Modica, P., Orthous-Daunay, F.-R., Rynö, J., Schulz, R., Silén, J., Thirkell, L., Varmuza, K., Zaprudin, B., Kissel, J., and Hilchenbach, M.: Carbon-rich dust in comet 67P/Churyumov-Gerasimenko measured by COSIMA/Rosetta, *MNRAS*, 469, S712–S722, <https://doi.org/10.1093/mnras/stx2640>, 2017.
- Benneke, B. and Seager, S.: Atmospheric retrieval for super-earths: Uniquely constraining the atmospheric composition with transmission spectroscopy, *Astrophysical Journal*, 753, 100, <https://doi.org/10.1088/0004-637X/753/2/100>, 2012.
- Besse, S., Vallat, C., Barthelemy, M., Coia, D., Costa, M., De Marchi, G., Fraga, D., Grotheer, E., Heather, D., Lim, T., Martinez, S., Arviset, C., Barbarisi, I., Docasal, R., Macfarlane, A., Rios, C., Saiz, J., and Vallejo, F.: ESA's Planetary Science Archive: Preserve and present reliable scientific data sets, *Planet. Space Sci.*, 150, 131–140, <https://doi.org/10.1016/j.pss.2017.07.013>, 2018.
- Borovicka, J.: Two components in meteor spectra, *Planet. Space Sci.*, 42, 145–150, [https://doi.org/10.1016/0032-0633\(94\)90025-6](https://doi.org/10.1016/0032-0633(94)90025-6), 1994a.
- Borovicka, J.: Line identifications in a fireball spectrum, *A&AS*, 103, 83–96, 1994b.
- Borovička, J.: Spectroscopic Analysis of Geminid Meteors, in: *Proceedings of the International Meteor Conference, 26th IMC, Baresges, France, 2007*, pp. 42–51, 2010.
- Borovička, J., Koteš, P., Spurný, P., Boček, J., and Štork, R.: A survey of meteor spectra and orbits: evidence for three populations of Na-free meteoroids, *Icarus*, 174, 15–30, <https://doi.org/10.1016/j.icarus.2004.09.011>, 2005.
- Brownlee, D.: The Stardust Mission: Analyzing Samples from the Edge of the Solar System, *Annual Review of Earth and Planetary Sciences*, 42, 179–205, <https://doi.org/10.1146/annurev-earth-050212-124203>, 2014.
- Cepelcha, Z.: Determination of wave-lengths in meteor spectra by using a diffraction grating, *Bulletin of the Astronomical Institutes of Czechoslovakia*, 12, 246, 1961.
- Cepelcha, Z.: Spectral data on terminal flare and wake of double-station meteor No. 38421 (Ondřejov, April 21, 1963), *Bulletin of the Astronomical Institutes of Czechoslovakia*, 22, 219, 1971.
- Dubs, M. and Schlatter, P.: A practical method for the analysis of meteor spectra, *WGN, Journal of the International Meteor Organization*, 43, 94–101, 2015.
- Etheridge, D. A. and Russell, J. A.: The Spectrum of a Meteor from the 1966 Leonid Shower, *PASP*, 80, 550, <https://doi.org/10.1086/128676>, 1968.
- Foreman-Mackey, D.: corner.py: Scatterplot matrices in Python, *The Journal of Open Source Software*, 1, 24, <https://doi.org/10.21105/joss.00024>, 2016.
- Foreman-Mackey, D., Hogg, D. W., Lang, D., and Goodman, J.: emcee : The MCMC Hammer , *Publications of the Astronomical Society of the Pacific*, 125, 306–312, <https://doi.org/10.1086/670067>, 2013.

- Foreman-Mackey, D., Farr, W., Sinha, M., Archibald, A., Hogg, D., Sanders, J., Zuntz, J., Williams, P., Nelson, A., de Val-Borro, M., Erhardt, T., Pashchenko, I., and Pla, O.: emcee v3: A Python ensemble sampling toolkit for affine-invariant MCMC, *Journal of Open Source Software*, 4, 1864, <https://doi.org/10.21105/joss.01864>, 2019.
- Goodman, J. and Weare, J.: Ensemble samplers with affine invariance, *Communications in Applied Mathematics and Computational Science*, 5, 65–80, <https://doi.org/10.2140/camcos.2010.5.65>, 2010.
- Hadamcik, E., Lvasseur-Regourd, A. C., Hines, D. C., Sen, A. K., Lasue, J., and Renard, J. B.: Properties of dust particles in comets from photometric and polarimetric observations of 67P, *MNRAS*, 462, S507–S515, <https://doi.org/10.1093/mnras/stx030>, 2016.
- Herzberg, G.: *Molecular spectra and molecular structure. Vol.1: Spectra of diatomic molecules*, 1950.
- Jenniskens, P.: Quantitative meteor spectroscopy: Elemental abundances, *Advances in Space Research*, 39, 491–512, <https://doi.org/10.1016/j.asr.2007.03.040>, 2007.
- Jenniskens, P., Tedesco, E., Murthy, J., Laux, C., and Price, S.: Spaceborne ultraviolet 251–384 nm spectroscopy of a meteor during the 1997 Leonid shower, *MAPS*, 37, 1071–1078, <https://doi.org/10.1111/j.1945-5100.2002.tb00878.x>, 2002.
- Jenniskens, P., Gural, P., and Berdeu, A.: CAMSS: A spectroscopic survey of meteoroid elemental abundances, in: *Meteoroids 2013*, edited by Jopek, T. J., Rietmeijer, F. J. M., Watanabe, J., and Williams, I. P., pp. 117–124, 2014.
- Koschny, D. and Diaz del Rio, J.: Meteor Orbit and Trajectory Software (MOTS) - Determining the Position of a Meteor with Respect to the Earth Using Data Collected with the Software MetRec, *WGN, Journal of the International Meteor Organization*, 30, 87–101, 2002.
- Koschny, D., Bettonvil, F., Licandro, J., Lujt, C. v. d., Mc Auliffe, J., Smit, H., Svedhem, H., de Wit, F., Witasse, O., and Zender, J.: A double-station meteor camera set-up in the Canary Islands - CILBO, *Geoscientific Instrumentation, Methods and Data Systems*, 2, 339–348, <https://doi.org/10.5194/gi-2-339-2013>, 2013a.
- Koschny, D., Bettonvil, F., Licandro, J., Lujt, C. v. d., Mc Auliffe, J., Smit, H., Svedhem, H., de Wit, F., Witasse, O., and Zender, J.: A double-station meteor camera set-up in the Canary Islands - CILBO, *Geoscientific Instrumentation, Methods and Data Systems*, 2, 339–348, <https://doi.org/10.5194/gi-2-339-2013>, 2013b.
- Koschny, D., Mc Auliffe, J., Drolshagen, E., Bettonvil, F., Licandro, J., van der Lujt, C., Ott, T., Smit, H., Svedhem, H., Witasse, O., and Zender, J.: CILBO - Lessons learned from a double-station meteor camera setup in the Canary Islands, in: *Proceedings of the International Meteor Conference, Giron, France, 18-21 September 2014*, edited by Rault, J. L. and Roggemans, P., pp. 10–15, 2014.
- Koschny, D., Albin, T., Drolshagen, E., Drolshagen, G., Drolshagen, S., Koschny, J., Kretschmer, J., van der Lujt, C., Molijn, C., Ott, T., Poppe, B., Smit, H., Svedhem, H., Toni, A., de Wit, F., and Zender, J.: Current activities at the ESA/ESTEC Meteor Research Group, in: *International Meteor Conference Mistelbach, Austria*, p. 204, 2015a.
- Koschny, D., Albin, T., Drolshagen, E., Drolshagen, G., Drolshagen, S., Koschny, J., Kretschmer, J., van der Lujt, C., Molijn, C., Ott, T., Poppe, B., Smit, H., Svedhem, H., Toni, A., de Wit, F., and Zender, J.: Current activities at the ESA/ESTEC Meteor Research Group, in: *International Meteor Conference Mistelbach, Austria*, p. 204, 2015b.
- Koschny, D., Drolshagen, E., Drolshagen, S., Kretschmer, J., Ott, T., Drolshagen, G., and Poppe, B.: Flux densities of meteoroids derived from optical double-station observations, *Planet. Space Sci.*, 143, 230–237, <https://doi.org/10.1016/j.pss.2016.12.007>, 2017.
- Koschny, D., Soja, R. H., Engrand, C., Flynn, G. J., Lasue, J., Lvasseur-Regourd, A.-C., Malaspina, D., Nakamura, T., Poppe, A. R., Sterken, V. J., and Trigo-Rodríguez, J. M.: Interplanetary Dust, Meteoroids, Meteors and Meteorites, *Space Sci. Rev.*, 215, 34, <https://doi.org/10.1007/s11214-019-0597-7>, 2019.

- Koschny, D. V., McAuliffe, J., Bettonvil, F. C. M., Gritsevich, M., van der Looij, C., Ocaña, F., Smit, H., Svedhem, H., and Zender, J. J.:
665 What happened at ESA's Meteor Research Group in 2010/11?, in: Proceedings of the International Meteor Conference, 30th IMC, Sibiu,
Romania, 2011, pp. 57–60, 2012.
- Lang, D., Hogg, D. W., Mierle, K., Blanton, M., and Roweis, S.: Astrometry.net: Blind Astrometric Calibration of Arbitrary Astronomical
Images, *AJ*, 139, 1782–1800, <https://doi.org/10.1088/0004-6256/139/5/1782>, 2010.
- Levasseur-Regourd, A.-C., Agarwal, J., Cottin, H., Engrand, C., Flynn, G., Fulle, M., Gombosi, T., Langevin, Y., Lasue, J., Mannel, T.,
670 Merouane, S., Poch, O., Thomas, N., and Westphal, A.: Cometary Dust, *Space Sci. Rev.*, 214, 64, <https://doi.org/10.1007/s11214-018-0496-3>, 2018.
- Loehle, S., Eberhart, M., Zander, F., Meindl, A., Rudawska, R., Koschny, D., Zender, J., Dantowitz, R., and Jenniskens, P.: Extension of the
plasma radiation database PARADE for the analysis of meteor spectra, *MAPS*, 56, 352–361, <https://doi.org/10.1111/maps.13622>, 2021.
- Madiedo, J. M.: Spectroscopy of a κ -Cygnid fireball afterglow, *Planet. Space Sci.*, 118, 90–94, <https://doi.org/10.1016/j.pss.2015.03.015>,
675 2015.
- Madiedo, J. M., Trigo-Rodríguez, J. M., Castro-Tirado, A. J., Ortiz, J. L., and Cabrera-Caño, J.: The Geminid meteoroid stream as a potential
meteorite dropper: a case study, *MNRAS*, 436, 2818–2823, <https://doi.org/10.1093/mnras/stt1777>, 2013.
- Matlovič, P., Tóth, J., Rudawska, R., Kornoš, L., and Pisarcíková, A.: Spectral and orbital survey of medium-sized meteoroids, *A&A*, 629,
A71, <https://doi.org/10.1051/0004-6361/201936093>, 2019.
- 680 Matlovič, P., Tóth, J., Kornoš, L., and Loehle, S.: On the sodium enhancement in spectra of slow meteors and the origin of Na-rich meteoroids,
Icarus, 347, 113817, <https://doi.org/10.1016/j.icarus.2020.113817>, 2020.
- Molau, S.: The Meteor Detection Software METREC, in: Proceedings of the International Meteor Conference, 17th IMC, Stara Lesna,
Slovakia, 1998, pp. 9–16, 1999.
- Pence, W. D., Chiappetti, L., Page, C. G., Shaw, R. A., and Stobie, E.: Definition of the Flexible Image Transport System (FITS), version
685 3.0, *A&A*, 524, A42, <https://doi.org/10.1051/0004-6361/201015362>, 2010.
- Ralchenko, Y. and Kramida, A.: Development of NIST Atomic Databases and Online Tools, *Atoms*, 8, 56,
<https://doi.org/10.3390/atoms8030056>, 2020.
- Rivilla, V. M., Drozdovskaya, M. N., Altwegg, K., Caselli, P., Beltrán, M. T., Fontani, F., van der Tak, F. F. S., Cesaroni, R., Vasyunin, A.,
Rubin, M., Lique, F., Marinakis, S., Testi, L., Rosina Team, Balsiger, H., Berthelier, J. J., de Keyser, J., Fiethe, B., Fuselier, S. A., Gasc,
690 S., Gombosi, T. I., Sémon, T., and Tzou, C. Y.: ALMA and ROSINA detections of phosphorus-bearing molecules: the interstellar thread
between star-forming regions and comets, *MNRAS*, 492, 1180–1198, <https://doi.org/10.1093/mnras/stz3336>, 2020.
- Rubin, M., Engrand, C., Snodgrass, C., Weissman, P., Altwegg, K., Busemann, H., Morbidelli, A., and Mumma, M.: On the Origin and
Evolution of the Material in 67P/Churyumov-Gerasimenko, *Space Sci. Rev.*, 216, 102, <https://doi.org/10.1007/s11214-020-00718-2>, 2020.
- Rudawska, R., Zender, J., Jenniskens, P., Vaubaillon, J., Kotten, P., Margonis, A., Tóth, J., McAuliffe, J., and Koschny, D.: Spectroscopic
695 Observations of the 2011 Draconids Meteor Shower, *Earth Moon and Planets*, 112, 45–57, <https://doi.org/10.1007/s11038-014-9436-8>,
2014.
- Rudawska, R., Zender, J., Koschny, D., Smit, H., Löhle, S., Zander, F., Eberhart, M., Meindl, A., and Latorre, I. U.: A spec-
troscopy pipeline for the Canary island long baseline observatory meteor detection system, *Planet. Space Sci.*, 180, 104773,
<https://doi.org/10.1016/j.pss.2019.104773>, 2020.
- 700 Russell, J. A., Sadoski, Michael J., J., Sadoski, D. C., and Wetzel, G. F.: The Spectrum of a Geminid Meteor, *PASP*, 68, 64,
<https://doi.org/10.1086/126881>, 1956.

- Smith, A. J.: Plasma radiation database parade v2.2, Technical Report TR 28/96 Issue 3., Tech. rep., Emsworth, UK: Fluid Gravity Engineering Ltd., 2006.
- Snodgrass, C., A'Hearn, M. F., Aceituno, F., Afanasiev, V., Bagnulo, S., Bauer, J., Bergond, G., Besse, S., Biver, N., Bodewits, D., Boehn-
705 hardt, H., Bonev, B. P., Borisov, G., Carry, B., Casanova, V., Cochran, A., Conn, B. C., Davidsson, B., Davies, J. K., de León, J., de Mooij, E., de Val-Borro, M., Delacruz, M., DiSanti, M. A., Drew, J. E., Duffard, R., Edberg, N. J. T., Faggi, S., Feaga, L., Fitzsimmons, A., Fujiwara, H., Gibb, E. L., Gillon, M., Green, S. F., Guijarro, A., Guilbert-Lepoutre, A., Gutiérrez, P. J., Hadamcik, E., Hainaut, O., Haque, S., Hedrosa, R., Hines, D., Hopp, U., Hoyo, F., Hutsemékers, D., Hyland, M., Ivanova, O., Jehin, E., Jones, G. H., Keane, J. V., Kelley, M. S. P., Kiselev, N., Kleyna, J., Kluge, M., Knight, M. M., Kokotanekova, R., Koschny, D., Kramer, E. A., López-Moreno, J. J.,
710 Lacerda, P., Lara, L. M., Lasue, J., Lehto, H. J., Lvasseur-Regourd, A. C., Licandro, J., Lin, Z. Y., Lister, T., Lowry, S. C., Mainzer, A., Manfroid, J., Marchant, J., McKay, A. J., McNeill, A., Meech, K. J., Micheli, M., Mohammed, I., Monguío, M., Moreno, F., Muñoz, O., Mumma, M. J., Nikolov, P., Opitom, C., Ortiz, J. L., Paganini, L., Pajuelo, M., Pozuelos, F. J., Protopapa, S., Pursimo, T., Rajkumar, B., Ramanjooloo, Y., Ramos, E., Ries, C., Riffeser, A., Rosenbush, V., Rousselot, P., Ryan, E. L., Santos-Sanz, P., Schleicher, D. G., Schmidt, M., Schulz, R., Sen, A. K., Somero, A., Sota, A., Stinson, A., Sunshine, J. M., Thompson, A., Tozzi, G. P., Tubiana, C., Villanueva,
715 G. L., Wang, X., Wooden, D. H., Yagi, M., Yang, B., Zaprudin, B., and Zegmott, T. J.: The 67P/Churyumov-Gerasimenko observation campaign in support of the Rosetta mission, *Philosophical Transactions of the Royal Society of London Series A*, 375, 20160249, <https://doi.org/10.1098/rsta.2016.0249>, 2017.
- Vaubailion, J., Koten, P., Margonis, A., Toth, J., Rudawska, R., Gritsevich, M., Zender, J., McAuliffe, J., Pautet, P.-D., Jenniskens, P.,
720 Koschny, D., Colas, F., Bouley, S., Maquet, L., Leroy, A., Lecacheux, J., Borovicka, J., Watanabe, J., and Oberst, J.: The 2011 Draconids: The First European Airborne Meteor Observation Campaign, *Earth Moon and Planets*, 114, 137–157, <https://doi.org/10.1007/s11038-014-9455-5>, 2015.
- Vicinanza, S., Koschny, D., Rudawska, R., Stam, D., van der Wal, W., and Zender, J.: Spectral Calibration of Meteors: An Elevation-
Dependent Atmospheric Correction, *WGN, Journal of the International Meteor Organization*, 49, 201–210, 2021.
- Vojáček, V., Borovička, J., Koten, P., Spurný, P., and Štork, R.: Properties of small meteoroids studied by meteor video observations, *A&A*,
725 621, A68, <https://doi.org/10.1051/0004-6361/201833289>, 2019.
- Ward, W.: Video meteor spectroscopic and orbital observations, 2015 April to 2016 April, *Journal of the British Astronomical Association*,
127, 217–222, 2017.
- Zender, J.: Line identifications in a fireball spectrum, *A&AS*, 103, 83–96, 1994.
- Zender, J.: CILBO Meteor Spectra Database., <https://doi.org/10.57780/esa-tfxgu7>, 2023.
- 730 Zender, J., Koschny, D., and Ravensberg, K.: Calibration of spectral video observations in the visual: theoretical overview of the ViDAS calibration pipeline, in: *Proceedings of the International Meteor Conference, Poznan, Poland, 22-25 August 2013*, edited by Gyssens, M., Roggemans, P., and Zoladek, P., pp. 126–129, 2014.
- Zender, J. J., Witasse, O., Koschny, D. V., Trautner, R., Knöfel, A., Diaz del Rio, J., and Quicke, G.: First results of spectroscopic measurements during the ESA Leonid campaign 2001, in: *Asteroids, Comets, and Meteors: ACM 2002*, edited by Warmbein, B., vol. 500 of *ESA Special Publication*, pp. 121–125, 2002.
- 735